

Rotibot: Use of Rotifers as Self-Propelling Biohybrid Microcleaners

Fernando Soto, Miguel Angel Lopez-Ramirez, Itthipon Jeerapan, Berta Esteban-Fernandez de Avila, Rupesh Kumar Mishra, Xiaolong Lu, Ingrid Chai, Chuanrui Chen, Daniel Kupor, Amir Nourhani, and Joseph Wang*

Self-propelled biohybrid microrobots, employing marine rotifers as their engine, named “rotibot,” are presented and their practical utility and advantages for environmental remediation are demonstrated. Functionalized microbeads are attached electrostatically within the rotifer mouth and aggregated inside their inner lip. The high fluid flow toward the mouth, generated by the strokes of rotifer cilia bands, forces an extremely efficient transport of the contaminated sample over the active surfaces of the functionalized microbeads. The reactive particles confined around the rotifer’s lip are thus exposed to a high flow rate of the pollutant solution, resulting in dramatically accelerated decontamination processes, without external mixing or harmful fuels. Theoretical simulations, modeling the greatly enhanced fluid dynamic associated with such built-in mixing effect, correlate well with the experimental observations. The rotibot thus proves to be an effective, versatile, and robust dynamic microcleaning platform for removing diverse environmental pollutants. Microbeads functionalized with lysozyme and organophosphorus hydrolase enzymes are shown to be extremely useful for enzymatic biodegradation of *Escherichia coli* and the nerve agent methyl paraoxon, respectively, while ligand (*meso*-2,3-dimercaptosuccinic acid) modified beads are used for removing heavy metal contaminants. Rotifer-based biohybrid microrobots hold considerable promise as self-propelling dynamic pumps for diverse large-scale environmental remediation applications.

1. Introduction

Microrobots^[1–7] are potentially promising tools for environmental remediation, specifically for accelerated decontamination of biological and chemical pollutants from water resources.^[8–11] The state-of-the-art motile microrobots have proven successful for the enhanced degradation of aqueous pollutants at the

F. Soto, M. A. Lopez-Ramirez, I. Jeerapan,
Dr. B. Esteban-Fernandez de Avila, Dr. R. K. Mishra, Dr. X. Lu,
I. Chai, Dr. C. Chen, D. Kupor,
Dr. A. Nourhani, Prof. J. Wang
Department of Nanoengineering
University of California
San Diego, La Jolla, CA 92093, USA
E-mail: josephwang@ucsd.edu

 The ORCID identification number(s) for the author(s) of this article can be found under <https://doi.org/10.1002/adfm.201900658>.

DOI: 10.1002/adfm.201900658

laboratory scale, overcoming the slow pollutant diffusion and absorption rates by reactive materials common to passive remediation methods. A major challenge in the field is to translate and scale up these microrobotic applications to relevant environmental settings by addressing limitations associated with toxic chemical fuels,^[12–21] short time span,^[22–24] and the small domain operation of externally-actuated microrobots.^[25–29] One plausible solution is to develop biohybrid microrobots^[30–35] that integrate self-propelling microorganisms with functionalized synthetic nanostructures. The current generation of biohybrid platforms is based primarily on flagellated microorganisms^[36–43] which survive only in delicate living conditions and may not provide sufficient fluid mixing for enhancing decontamination processes. Moreover, while enzymatically powered micropumps^[44,45] have been utilized to generate fluid mixing, they are tailored to operate under specific environmental conditions and with their respective substrates.

We report here on biohybrid microrobots whose operation can be scaled up to realistic aqueous environmental settings. Among the microorganism candidates, we selected the marine rotifer (*Brachionus*, size $\approx 100\text{--}300\ \mu\text{m}$) and hence named the resulting biohybrid microrobot “rotibot.” Over millions of years, rotifers have adapted to and harvest their energy from their environments (e.g., puddles, rivers, lakes, and ocean).^[46,47] They rely on the beating of their cilia bands to control the fluid flow for efficient locomotion and feeding. The microorganism engine of the resulting rotibots thus mixes the solution locally and transports it efficiently toward its functionalized mouth. The rotifer not only can serve as an extremely efficient self-propulsion engine of the biohybrid microrobot, but can also integrate sensing capabilities that respond to environmental signals and maneuver effectively in their environment.^[48–51]

We engineered the rotibot as a self-propelling microcleaner by exploiting the negative charge on its cilia surface for confining positively-charged functional particles. The generated flow field transports the functional microbeads toward the

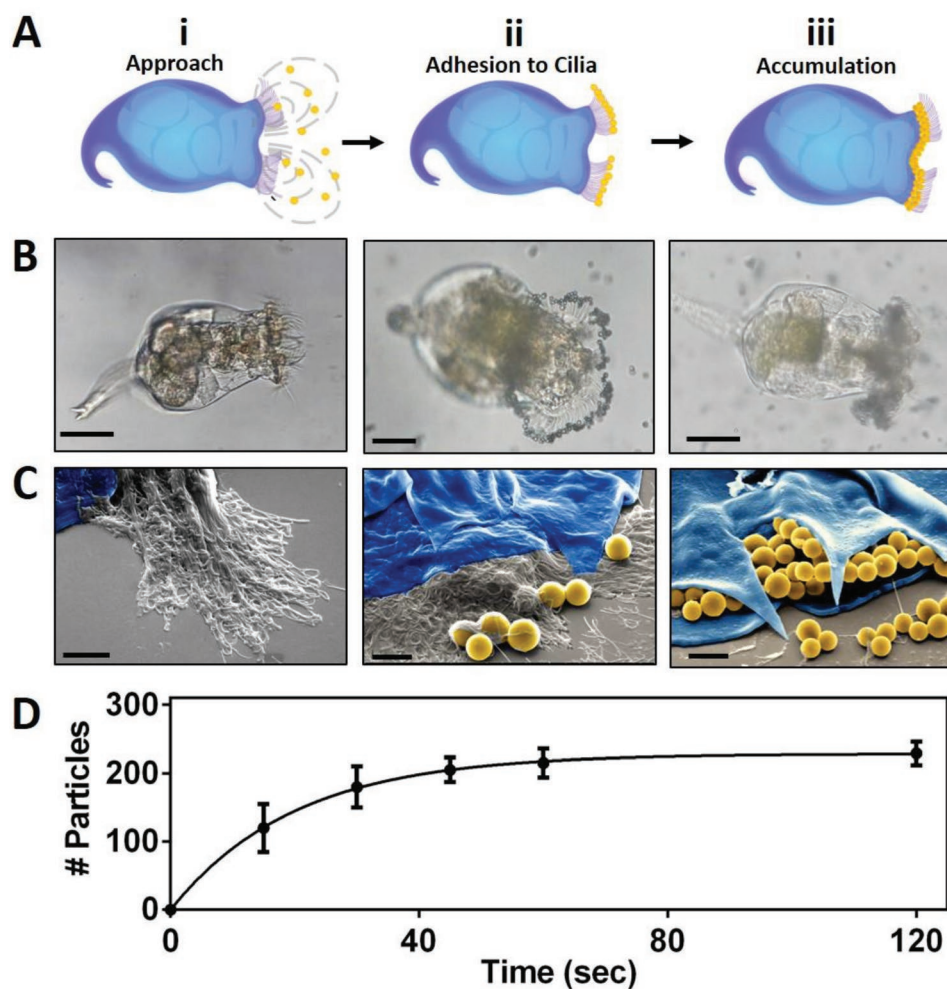


Figure 1. Mechanism for the formation of the rotibot: A) scheme, B) microscopy images, and C) scanning electron microscopy images, illustrating the steps toward rotifer (blue) uptake of the functionalized microbeads (yellow). i) Microbeads approaching the rotifer's mouth due to a strong directional flow, ii) upon contact with the cilia the beads adhere in their tips, and iii) the cilia within the inner lips of the rotifer accumulate the particles in that location and frees up the cilia for subsequent adhesion. D) Time dependence of the microbead accumulation in the rotibot's mouth ($n = 5$). Scale bars: B: 50 μm ; C: 5 μm .

mouth and accumulating them underneath the lips (Figure 1). The numerous cilia outside the mouth, actuating in a coordinated cilia-stroke pattern, generate a vortex flow field near the rotibot head. The flow streamlines are closely dominated by the operation modes of the rotifer, e.g., moving or feeding, and contribute to highly efficient solution mixing around the rotibot. The experimentally observed flow streamlines correlate well with our theoretical simulations.

We fine-tuned the active decontamination sites on the microbeads to create specialized reactive microcleaner toward a dramatically accelerated pollutant degradation. Three examples of environmental remediation applications were used to demonstrate the remarkable efficiency and versatility of the new rotibot microcleaners. Lysozyme and organophosphorus hydrolase (OPH) tagged microbeads have thus been used for illustrating the enhanced enzymatic biodegradation of *Escherichia coli* and the nerve agent methyl paraoxon, respectively. We also used ligand-modified meso-2,3-dimercaptosuccinic acid (DMSA) Janus microbeads for improved chelation

and removal of heavy metal contaminants. The high flow rate toward the mouth forces efficient transport of the pollutant solution over the reactive microbead aggregate structures that rapidly degrade the transported pollutants. Such remediation is realized in the absence of harmful fuels or external stirring, and with relative high speeds and low cost that indicate promise for scaling up cleanup processes. Our results thus illustrate that coupling functionalized nanostructures and marine rotifer offers tremendous promise for developing self-propelling fuel-free microcleaners for large-scale remediation action toward diverse environmental applications.

2. Results and Discussion

The rotibots were fabricated by absorbing positively-charged microbeads on the negatively-charged surface of the rotifer's cilia^[48,49] and subsequently accumulating the microbeads underneath the lips via particle trapping. Figure 1 illustrates

the attachment of the beads to the rotifer lips, by intermediate steps: i) transport of the microbeads toward the cilia bands due to the strong flow field toward the rotifer mouth, ii) absorption of the microbeads onto the cilia, and iii) accumulation of the beads onto the rough surface of the inner mouth lip, (Figure S1, Supporting Information) serving as a pocket that traps the microbeads. These accumulation steps are illustrated in the scheme of Figure 1A, the microscopy images of Figure 1B, and scanning electron microscopy (SEM) images of Figure 1C. The strong electrostatic interactions between the cilia's negative charge ($\zeta = -12.4$ mV) and the positively-charged microbeads ($\zeta = +59$ mV) lead to the physical binding of microbeads to the cilia. On an average, the rotifer's mouth is saturated with the microbeads within ≈ 120 sec (see Figure 1D). While small particles were accumulated successfully inside the rotifer mouth, particles larger than $4 \mu\text{m}$ did not show any long-lasting attachment. To study the localization of the microbead adhesion inside the rotifer mouth, we also relied on positively-charged fluorescent beads coated with a polydopamine layer^[40,52] (Figure S2, Supporting Information). While some microbeads are dislodged upon the rapid movement of the rotibots, the majority of the microbeads remained firmly trapped in the mouth over long periods (>30 min). No microbead attachment was observed on other parts of the rotibot body. Control experiments using negatively-charged (carboxylated) microbeads and neutral polystyrene

microbeads indicated negligible bead attachment to the rotifer's mouth, thereby supporting the importance of the electrostatic accumulation of the charged beads.

The locomotion of rotibot is based on the rotifers' coordinated strokes of cilia bands, which induce a tangential flow field near the head. The cilia movement involves repeated cycles of power and recovery strokes, as shown in the time-lapse micrographs in Figure S3 and Video S1 in the Supporting Information. The generated flow streamlines are closely dominated by the rotifer's operation mode, such as moving or feeding, etc.^[52–55] The translocation of free-swimming rotibots allows them to transport active materials while generating disordered open streamlines and providing efficient local mixing. Figure 2 examines the rotibot enabled fluid mixing and hydrodynamics. Figure 2A displays track lines of a rotibot and a bare rotifer over a 4 s period, while Figure 2B shows the bar charts, corresponding to the average speed. The functional rotibots display a slightly lower speed (of $179 \pm 23 \mu\text{m s}^{-1}$) compared to the bare rotifers ($236 \pm 12 \mu\text{m s}^{-1}$). Such rotibot movement results in higher mixing and hence significantly enhances the mass transport for decontamination. We deduced this fact by analyzing the mean-squared displacement of tracer particles and comparing with the mean-squared displacement of these particles undergoing Brownian motion, and also tracer particles in the vicinity of flagellated microorganisms or chemically-propelled synthetic microrockets, as shown in Figure 2C.

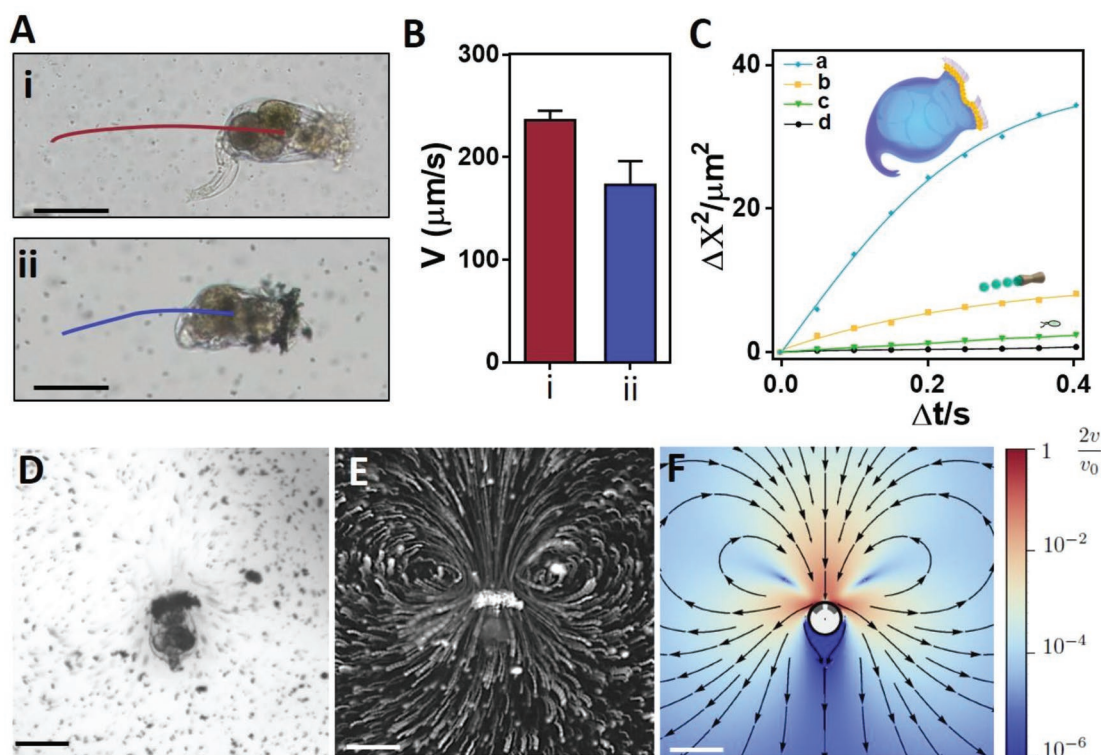


Figure 2. Rotibot enabled fluid mixing and hydrodynamics. A) Images illustrating the movement of i) bare rotifer and ii) rotibot during 4 s tracking lines. B) Average speed of the rotifer before and after modification ($n = 5$). C) Mean squared displacement of $3 \mu\text{m}$ tracer particles produced by a) freely swimming rotibot, b) chemically propelled synthetic microrocket, c) flagellated microorganism, and d) Brownian motion. D) Bright-field optical microscopy of a stationary rotibot in a solution containing functionalized fluorescent microbeads. E) Visualization of vortices generated by overlapping a stack of 30 fluorescence microscopy images, corresponding to 1 sec of the same rotibot. F) Simulation of the flow field generated by a rotibot, illustrating the significant faster fluid flow near the mouth in units of maximum speed created by cilia around the rotifer. Scale bars: D–F: $100 \mu\text{m}$.

The rotibots exhibit adaptive self-locomotion and survival in diverse aqueous environments over long periods including pond water ($104 \pm 32 \mu\text{m s}^{-1}$), residual water ($163 \pm 21 \mu\text{m s}^{-1}$), lake water ($175 \pm 24 \mu\text{m s}^{-1}$), pool water ($176 \pm 34 \mu\text{m s}^{-1}$), and seawater ($179 \pm 23 \mu\text{m s}^{-1}$). In addition, freely swimming rotibots can generate localized fluid mixing and swim against the direction of a flow current in confined channels. (Figure S4 and Video S2, Supporting Information). The fluid flow pattern around the rotibot changes as its rotifer engine changes from the swimming to the feeding modes. Figure 2D (taken from Video S3 in the Supporting Information) shows the bright field microscopy image of a stationary rotibot (attached to the surface) in the feeding mode with fluorescent microbeads coated with a polydopamine layer. Figure 2E overlaps a stack of 30 fluorescent microscopy images (during a 1 sec period) of the same rotibot. The visualized vortices are attributed to the effect of boundaries and confinement near the rotibot. For a typical microswimmer of length $\approx 150 \mu\text{m}$ and tracer particle speed $\approx 150 \mu\text{m s}^{-1}$ in water with density 1000 kg m^{-3} and viscosity $8.90 \times 10^{-4} \text{ Pa}\cdot\text{s}$, the Reynold number is ≈ 0.08 . Thus, the flow velocity field v follows Stokes equation

$$\mu \nabla^2 v = \nabla p \text{ and } \nabla \cdot v = 0 \quad (1)$$

The rotibot is bound to swim between two parallel horizontal glass slides and the cilia bands could generate tangential flow near the rotibot head, leading to a velocity field v_x (on the rotibot surface of $\approx 451 \mu\text{m s}^{-1}$). The details of the model and solution^[54] are provided and explained in the Supporting Information and Figure S5 in the Supporting Information. The resulting flow field is shown in Figure 2F. Such simulation of the flow field generated by a rotibot illustrates the significant faster fluid flow near the mouth in units of maximum speed created by cilia around the rotifer. The effect of confinement and the tangential flow thus leads to the formation of vortices that are responsible for large particle displacement and efficient local mixing, as observed experimentally in the supporting videos in the Supporting Information. The microbead aggregates thus have a significantly higher rate of exposure to solutes in the fluid, compared to microbeads suspended in the solution. Such remarkable pumping action toward the mouth forces efficient solution transport toward the confined reactive microbead aggregate structures and will be used in the following sections toward accelerated remediation processes without added fuel or external mixing.

The remarkably enhanced fluid dynamic associated with the rotibot platform offers considerable promise for increasing the efficiency of a variety of decontamination processes. The major benefits of such built-in sample solution mixing have been illustrated

toward the decontamination of diverse environmental pollutants, including bacteria (*E. coli*), nerve agent (methyl paraoxon), and heavy metal ions (Cd and Pb) from aqueous solution. Such greatly enhanced decontamination has been realized by functionalizing the microbeads with enzymes or chelating agents, which serve as active sites for specific remediation tasks. The rotifer exposure to the different pollutants did not affect their movement or viability during the experiments.

The rotibots were evaluated initially as potential antibacterial microcleaners. For this purpose, microbeads were functionalized with lysozyme enzymes capable of cleaving glycosidic bonds of peptidoglycans present in the cell wall of different bacteria.^[29,56] Details of the functionalization protocols of the microbeads are described in the experimental section. Figure 3A displays a schematic of the lysozyme-modified microbeads attached to the rotibot. The mixing effect of the directed flow field produced near the rotibot's mouth lead to intensified bacteria-lysozyme contacts and to a greatly improved antibacterial efficiency. Figure 3B shows SEM images of *E. coli*, taken before and after a 5 min treatment with the lysozyme-modified

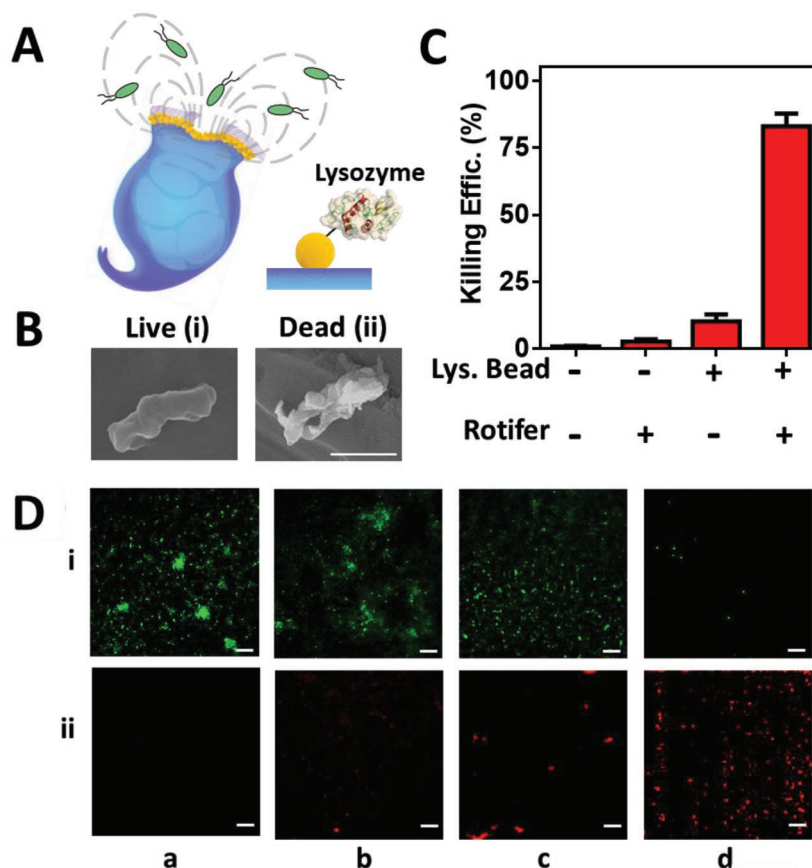


Figure 3. Lysozyme-modified rotibot-based antibacterial treatment. A) Schematic illustration of lysozyme microbeads responsible for killing *E. coli* bacteria. B) SEM micrographs illustrating i) live *E. coli* and ii) dead *E. coli* before and after the treatment with lysozyme-modified rotifers, respectively. Scale bars: $2 \mu\text{m}$. C) Statistical plot showing the *E. coli* bacteria killing efficiency by the different treatment conditions. D) Fluorescence images illustrating live (in green, top) and dead (in red, bottom) *E. coli* after 5 min treatment under different conditions including negative control, bare rotifer, lysozyme microbeads, and lysozyme-modified rotibot. a–d) Scale bars: $50 \mu\text{m}$. Experimental conditions: bacteria, $9.2 \times 10^9 \text{ CFU mL}^{-1}$; rotifer, 20 units per control; antibacterial treatment time, 5 min.

rotibot. These images illustrate a notable change in bacteria morphology upon degradation of the bacteria membrane. The antibacterial capacity of the rotibots was quantified using a bacterial viability commercial kit, based on the use of two dyes that estimate the numbers of viable and nonviable bacteria. We compared the antibacterial efficiency under different experimental conditions, negative control, bare rotifers, lysozyme microbeads, and lysozyme-modified rotibots. The bacterial-killing efficiency of each experimental condition is illustrated in the graph of Figure 3C. While there was a negligible bactericidal effect using the water alone (0%) and bare rotifers (1%) controls, the biohybrid approach results in an eightfold higher bacteria killing efficiency (83%), compared to the lysozyme microbeads alone (10.2%). The fluorescent images of Figure 3D illustrate the total of living *E. coli* (i, in green) and dead *E. coli* (ii, in red), obtained after the corresponding treatment. The rotibot facilitated the elimination of most of the bacteria population within less than 5 min (d), compared to the high bacteria survival rate observed in different control experiments (a–c).

The versatility of the new rotibots decontamination platform was illustrated also toward biocatalytic degradation of organophosphorus pesticides. Such rotibot-based accelerated enzymatic treatment processes relied on the use of OPH functionalized microbeads in connection to the organophosphorus methyl paraoxon.^[57] Figure 4Ai displays a schematic of the OPH-modified microbead attached to the rotibot. Electrochemical square-wave voltammetry (SWV) technique was used to measure the nitro-phenolic byproduct of the OPH enzyme hydrolyzation of methyl paraoxon.^[58,59] The voltammograms

in Figure 4Aii represent different incubation conditions with a methyl paraoxon solution, including a) negative control, b) bare rotifers, c) static OPH–microbeads, and (d) OPH-modified rotibots. The nitro-phenol voltammetric peak, observed at +0.795 V, is proportional to the amount of hydrolyzed nerve agent, and thus reflects the efficiency of the methyl paraoxon degradation process under the different treatment conditions, as summarized in the graph bar of Figure 4Aiii. The OPH biocatalytic degradation efficiency increased significantly (by eightfold) using rotibots when compared to static OPH–microbeads (29.6 vs 3.6 μA , respectively).

The new rotibots platform also offers a significant improvement in the removal of heavy metals from polluted water, in connection to rotifers modified with DMSA-functionalized Janus beads. The scheme in Figure 4Bi shows the mechanism of heavy metal removal by the DMSA ligand via metal chelation.^[60] Cadmium and lead concentrations were measured simultaneously using anodic stripping SWV which can detect traces of heavy metals. The advantages of the DMSA-functionalized rotibot were illustrated by incubating the heavy metal solution for 30 min with a) negative control/buffer, b) bare rotifers, c) only DMSA-functionalized beads, and (d) DMSA-modified rotibots. The resulting SWVs, shown in Figure 4Bii, display two distinct oxidation peaks. The successful simultaneous detection of two heavy metals displays a large peak-to-peak separation between the stripping peaks at -0.85 and -0.50 V, corresponding to Cd^{2+} and Pb^{2+} ions, respectively. These peak current signals are proportional to the heavy metal solution concentrations. Figure 4Biii and iv illustrate the removal

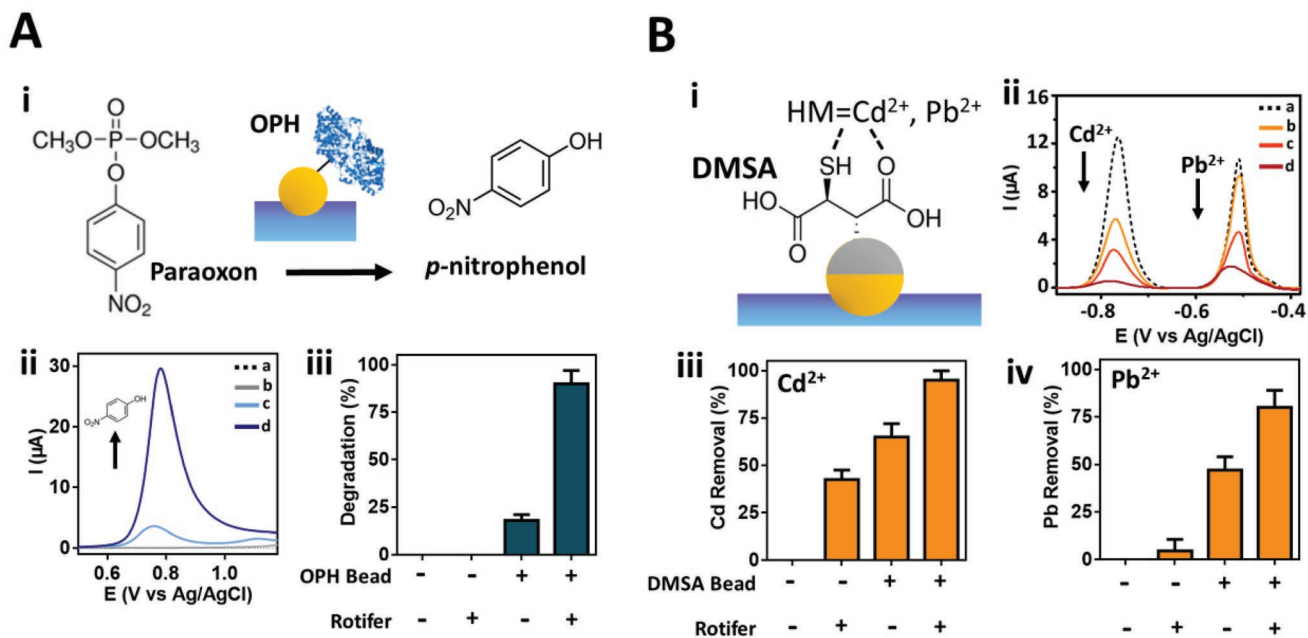


Figure 4. Use of rotibots for chemical pollutant remediation. A) OPH–microbeads modified rotibots for nerve agent decontamination. i) Schematic illustrating the OPH-based degradation of methyl paraoxon. ii) Square wave voltammetry (SWV) for decontamination after negative control, bare rotifer, OPH–microbeads, and OPH-modified rotibot a–d). iii) Statistical plot showing the degradation efficiency by the different treatments ($n = 5$). B) DMSA-Janus microbeads modified rotibots for heavy metal removal. i) Schematic illustrating DMSA-based chelation of heavy metals. ii) SWVs for Cd^{2+} and Pb^{2+} presence after negative control, bare rotifer, DMSA-microbeads, and DMSA-modified rotibot. a–d) Statistical plot showing the removal efficiency of iii) Cd^{2+} and iv) Pb^{2+} by the different treatments ($n = 3$).

efficiency of Cd²⁺ and Pb²⁺ by the DMSA-functionalized rotifer. The hybrid rotifer offers a significantly higher heavy metal removal efficiency compared to unmodified rotifers or static DMAS particles. The unmodified rotifers also presented some metal removal capability due to absorption of heavy metals into their body. Overall, the rotibots presented a substantially higher heavy metal removal when compared to bare rotifers or to the DMSA particles combined, suggesting a favorable synergistic effect of the large-scale mixing, rather than additive results.

3. Conclusions

We have presented the use of biohybrid rotibots as efficient environmental microcleaners, with marine rotifers serving as the engine of the microrobot. Functionalized microbeads have been confined within the rotifer mouth via electrostatic interaction and particle trapping. The reactive microbeads are subjected to a remarkably high localized fluidic flow, generated by the cilia strokes, that leads to greatly enhanced decontamination processes. Such operation is realized in the absence of external mixing force or harmful fuels, and with relative high speeds and low cost those indicate promise for scaling up remediation processes. The experimentally observed rotifer-enhanced fluid dynamics correlates well with theoretical simulations. Such intrinsic and effective micropumping action toward the entrapped functionalized microbeads results in efficient decontamination processes, as was demonstrated toward diverse environmental pollutants, including *E. coli* bacteria, OP nerve agents and heavy metals such as lead or cadmium. Future decontamination efforts should replace the plastic (latex and polystyrene) microbeads, utilized in this proof-of-concept study, with biodegradable functional microparticles. Such ability to modify and functionalize microorganisms introduces new possibilities for preparing ecofriendly biobots and to accelerate a wide range of decontamination processes. Such application would benefit also from the microswimmer response to certain biomolecules, such as caffeine, that increases their velocity (Figure S6, Supporting Information), which could prove beneficial for diverse applications. The rotifer biohybrid platform thus holds a considerable promise for environmental remediation and defense neutralization applications.

4. Experimental Section

Marine Rotifer Preparation and Recording: Marine rotifers (*Brachionous*) were purchased from Carolina Biological Supply and used without further treatment. A stock solution was cultured using an ocean water sample collected at La Jolla, California. Rotifers were collected from the stock culture and diluted into aliquots containing ≈40 rotifers mL⁻¹. To record the motion of Rotifers, images and videos were taken in an inverted optical microscope (Nikon Eclipse Instrument Ti-S), coupled with 4×, 10×, and 20× objectives, and a Hamamatsu digital camera C11440 and FrameLink Express software. NIS elements software was used to measure rotifer locomotion speed and mean squared displacement of tracer particles. For propulsion experiments in different media, the rotifers were collected using an extended pipet tip (20 μL) and placed in 200 μL of the different studied media. To calculate the mean square displacement under which different microswimmers were produced, 1 μm polystyrene microbeads were used and their mixing capabilities

were measured, including displacement under Brownian motion, locomotion of platymonas (Carolina Biological Supply), and locomotion of bubble propelled chemical microrockets, synthesized using template electrodeposition^[61] and under rotifer Locomotion.

Microbead Surface Coating: Carboxylated fluorobeads with 1 μm in diameter (Spherotech cat no, cfp-0856-2) were used as a model for particle attachment to rotifer body. The attachment relies on electrostatic interaction. Three different coatings were used in this work. Firstly, the beads were coated with a positive charge polydopamine layer, which consisted of incubating the beads overnight with a dopamine solution (2 mg dopamine L⁻¹ of 10 × 10⁻³ M tris, pH 8.5).^[52] These beads were then incubated with marine rotifer for 30 min before evaluation of attachment. Fluorescence imaging was performed using a B2 filter which allows differentiating the fluorobead and the rest of rotifer. The particle displacement image stacking was performed using Image J software and Flow trace plug in.^[62] The enzymes lysozyme and organophosphorus hydrolase were functionalized into the carboxylated fluorobeads, via activation of the carboxylic moieties using a NHS (20 × 10⁻³ M)/EDC (10 × 10⁻³ M) in 0.1 M MES buffer (pH 6.5) for 30 min. Next, the beads were washed and immersed in solutions containing 5 mg mL⁻¹ of lysozyme or 3.5 mg mL⁻¹ of organophosphorus hydrolase.

Bacteria Killing: The antibacterial activity of rotibots was examined by analyzing *E. coli* bacteria cells (from Sigma-Aldrich, St Louis, 384 MO). *E. coli* bacteria (9.2 × 10⁹ CFU mL⁻¹) was mixed with 20 rotibots and lysozyme modified microbeads. The mixture was allowed to react for 5 min, and after that, the mixture was centrifuged at 14 000 rpm for 10 min to isolate the bacteria pellet. The pellet was resuspended in 100 μL of a mix of Syto-9 dye and propidium iodide dye previously dissolved in water following the specifications of the L13152 LIVE/DEAD BacLight Bacterial Viability Kit (from Thermo Fisher Scientific). Microtubes were covered with aluminum foil and gently mixed for 20 min. Subsequently, they were centrifuged (14 000 rpm for 10 min) and the pellet was resuspended in 100 μL of water for counting, taking 2 μL aliquots for obtaining the fluorescence images. All other control experiments were analyzed following the same protocol.

Nerve Agent Decontamination: The nerve agent decontamination activity was examined using 20 rotibots based on OPH-functionalized microbeads. Firstly, 40 μL of each solution (including 100 ng OPH solution) were incubated with 40 μL of methyl paraoxon. The biocatalytic degradation of the pesticide to *p*-nitro phenol was monitored by applying square wave voltammetry over the potential range from +0.30 to +1.20 V (vs Ag/AgCl), amplitude, 25 mV, and a frequency of 10 Hz. Control experiments indicated that neither the spheres nor the rotifers alone resulted any degradation.

Heavy Metal Removal: Electrochemical experiments were carried out with a μAutolab Type II system, controlled by NOVA software version 1.11. The three-electrode system was performed in a batch system. The three electrodes consist of conventional glassy carbon (GCE), Ag/AgCl (3 M KCl), and Pt electrodes as the working (WE), reference (RE), and counter (CE) electrodes, respectively. The GCE was polished using 3–4 μm with Al₂O₃ powder and then rinsed with ultrapure water. The electrode was then immersed in 1 M HNO₃ for 5 min to fully remove metal residues.

The square wave anodic stripping voltammetry detection was performed in a 1.5 mL electrochemical cell, containing 0.1 M acetate buffer (pH 4.5), 1 mg L⁻¹ Bi³⁺, and amounts of Cd²⁺ and Pb²⁺. A concentration of 400 μg L⁻¹ was used in the experiment to study the removal of heavy metals under different experimental conditions. After incubation with the rotibots and control experiments, the solution was centrifuged, the supernatant was used to perform SWV in an electrochemical cell. The preconcentration was carried out at -1.4 V for 300 s under stirring where Bi³⁺ and the target analytes were simultaneously electrodeposited on the GCE surface. After the accumulation step, the stirring was stopped. The stripping voltammogram was then recorded by applying a SWV with a positive-going potential scan at a frequency of 10 Hz, an amplitude of 5 mV, and a potential step of 5 mV. The electrode was cleaned at +0.3 V for 180 s under stirring condition and followed by electrode polishing prior to the next experiment. All experiments were conducted at room temperature in air atmosphere.

Supporting Information

Supporting Information is available from the Wiley Online Library or from the author.

Acknowledgements

This work was supported by the Defense Threat Reduction Agency Joint Science and Technology Office for Chemical and Biological Defense (Grant Nos. HDTRA 1-16-1-0013). F.S. and M.A.L.-R. acknowledge fellowship from the UC MEXUS-CONACYT. I.J. acknowledge fellowship from the Thai Development and Promotion of Science and Technology Talents Project (DPST). The authors acknowledge Enrique Contreras for his assistance with ζ potential measurements; Mohammad Alsoraya and Emil Karshalev for their helpful discussion assistance with experiments.

Conflict of Interest

The authors declare no conflict of interest.

Keywords

biocatalytic degradation, biohybrid, environmental remediation, heavy metal removal, micropump, microswimmers, rotifer

Received: January 21, 2019

Revised: March 7, 2019

Published online:

- [1] J. Wang, *Nanomachines: Fundamentals and Applications*, Wiley-VCH, Weinheim, Germany **2013**.
- [2] W. Wang, W. Duan, S. Ahmed, T. E. Mallouk, A. Sen, *Nano Today* **2013**, *8*, 531.
- [3] M. Luo, Y. Feng, T. Wang, J. Guan, *Adv. Funct. Mater.* **2018**, *28*, 1706100.
- [4] C. Chen, F. Soto, E. Karshalev, J. Li, J. Wang, *Adv. Funct. Mater.* **2018**, *29*, 1806290.
- [5] L. K. Abdelmohsen, F. Peng, Y. Tu, D. A. Wilson, *J. Mater. Chem. B* **2014**, *2*, 2395.
- [6] K. Kim, J. Guo, Z. Liang, D. Fan, *Adv. Funct. Mater.* **2018**, *28*, 1705867.
- [7] P. Yáñez-Sedeño, S. Campuzano, J. Pingarrón, *Appl. Mater. Today* **2017**, *9*, 276.
- [8] J. Parmar, D. Vilela, K. Villa, J. Wang, S. Sánchez, *J. Am. Chem. Soc.* **2018**, *140*, 9317.
- [9] J. Orozco, L. A. Mercante, R. Pol, A. Merkoçi, *J. Mater. Chem. A* **2016**, *4*, 3371.
- [10] W. Gao, J. Wang, *ACS Nano* **2014**, *8*, 3170.
- [11] A. Nourhani, D. Brown, N. Pletzer, J. G. Gibbs, *Adv. Mater.* **2017**, *29*, 1703910.
- [12] B. Jurado-Sánchez, M. Pacheco, R. Maria-Hormigos, A. Escarpa, *Appl. Mater. Today* **2017**, *9*, 407.
- [13] J. G. S. Moo, M. Pumera, *Chem. - Eur. J.* **2015**, *21*, 58.
- [14] V. V. Singh, F. Soto, K. Kaufmann, J. Wang, *Angew. Chem., Int. Ed.* **2015**, *54*, 6896.
- [15] J. Parmar, D. Vilela, E. Pellicer, D. Esqué-de los Ojos, J. Sort, S. Sánchez, *Adv. Funct. Mater.* **2016**, *26*, 4152.
- [16] R. Kumar, M. Kiristi, F. Soto, J. Li, V. V. Singh, J. Wang, *RSC Adv.* **2015**, *5*, 78986.
- [17] S. K. Srivastava, M. Guix, O. G. Schmidt, *Nano Lett.* **2016**, *16*, 817.
- [18] Z. Lin, Z. Wu, X. Lin, Q. He, *Chem. - Eur. J.* **2016**, *22*, 1587.
- [19] T. Maric, C. C. Mayorga-Martinez, B. Khezri, M. Z. M. Nasir, X. Chia, M. Pumera, *Adv. Funct. Mater.* **2018**, *28*, 1802762.
- [20] R. Maria-Hormigos, B. Jurado-Sánchez, A. Escarpa, *Adv. Funct. Mater.* **2018**, *28*, 1704256.
- [21] H. Wang, M. G. Potroz, J. A. Jackman, B. Khezri, T. Marić, N.-J. Cho, M. Pumera, *Adv. Funct. Mater.* **2017**, *27*, 1702338.
- [22] C. Chen, E. Karshalev, J. Li, F. Soto, R. Castillo, I. Campos, F. Mou, J. Guan, J. Wang, *ACS Nano* **2016**, *10*, 10389.
- [23] D. Vilela, M. M. Stanton, J. Parmar, S. Sanchez, *ACS Appl. Mater. Interfaces* **2017**, *9*, 22093.
- [24] J. Li, V. V. Singh, S. Sattayasamitsathit, J. Orozco, K. Kaufmann, R. Dong, W. Gao, B. Jurado-Sánchez, Y. Fedorak, J. Wang, *ACS Nano* **2014**, *8*, 11118.
- [25] Q. Zhang, R. Dong, Y. Wu, W. Gao, Z. He, B. Ren, *ACS Appl. Mater. Interfaces* **2017**, *9*, 4674.
- [26] F. Soto, G. L. Wagner, V. Garcia-Gradilla, K. T. Gillespie, D. R. Lakshminpathy, E. Karshalev, C. Angell, Y. Chen, J. Wang, *Nanoscale* **2016**, *8*, 17788.
- [27] M. Hoop, Y. Shen, X. Z. Chen, F. Mushtaq, L. M. Iuliano, M. S. Sakar, A. Petruska, M. J. Loessner, B. J. Nelson, S. Pané, *Adv. Funct. Mater.* **2016**, *26*, 1063.
- [28] B. Esteban-Fernández de Ávila, P. Angsantikul, D. E. Ramírez-Herrera, F. Soto, H. Teymourian, D. Dehaini, Y. Chen, L. Zhang, J. Wang, *Sci. Rob.* **2018**, *3*, eaat0485.
- [29] M. Kiristi, V. V. Singh, B. Esteban-Fernández de Ávila, M. Uygun, F. Soto, D. A. Uygun, J. Wang, *ACS Nano* **2015**, *9*, 9252.
- [30] S. Palagi, P. Fischer, *Nat. Rev. Mater.* **2018**, *3*, 113.
- [31] H. Wang, M. Pumera, *Adv. Funct. Mater.* **2018**, *28*, 1705421.
- [32] K. Bente, A. Codutti, F. Bachmann, D. Fèvre, *Small* **2018**, *14*, 1704374.
- [33] Z. Hosseinidou, B. Mostaghaci, O. Yasa, B. W. Park, A. V. Singh, *Adv. Drug Delivery Rev.* **2016**, *106*, 27.
- [34] H. Xu, M. Medina-Sánchez, V. Magdanz, L. Schwarz, F. Hebenstreit, O. G. Schmidt, *ACS Nano* **2018**, *12*, 327.
- [35] M. Nagai, H. Asai, H. Fujita, *Mech. Eng. J.* **2014**, *1*, MN0038.
- [36] M. M. Stanton, B. W. Park, D. Vilela, K. Bente, D. Fèvre, M. Sitti, S. Sanchez, *ACS Nano* **2017**, *11*, 9968.
- [37] A. V. Singh, Z. Hosseinidou, B. W. Park, O. Yasa, M. Sitti, *ACS Nano* **2017**, *11*, 9759.
- [38] B. W. Park, J. Zhuang, O. Yasa, M. Sitti, *ACS Nano* **2017**, *11*, 8910.
- [39] O. Felfoul, M. Mohammadi, S. Taherkhani, D. De Lanauze, Y. Z. Xu, D. Loghini, S. Essa, S. Jancik, D. Houle, M. Lafleur, L. Gaboury, *Nat. Nanotechnol.* **2016**, *11*, 941.
- [40] M. M. Stanton, B. W. Park, A. Miguel-López, X. Ma, M. Sitti, S. Sánchez, *Small* **2017**, *13*, 1603679.
- [41] Y. Alapan, O. Yasa, B. Yigit, I. C. Yasa, P. Erkoc, M. Sitti, *Annu. Rev. Control Rob. Auton. Syst.* **2018**, *2*, <https://www.annualreviews.org/doi/pdf/10.1146/annurev-control-053018-023803>.
- [42] O. Yasa, P. Erkoc, Y. Alapan, M. Sitti, *Adv. Mater.* **2018**, *30*, 1804130.
- [43] F. Soto, R. Chrostowski, *Front. Bioeng. Biotechnol.* **2018**, *6*, 170.
- [44] S. Sengupta, D. Patra, I. Ortiz-Rivera, A. Agrawal, S. Shklyav, K. K. Dey, U. Córdova-Figueroa, T. E. Mallouk, A. Sen, *Nat. Chem.* **2014**, *6*, 415.
- [45] A. C. Hortelão, R. Carrascosa, N. Murillo-Cremaes, T. Patiño, S. Sánchez, *ACS Nano* **2019**, *13*, 429.
- [46] C. G. Wilson, P. W. Sherman, *Science* **2010**, *327*, 574.
- [47] A. Krisko, M. Leroy, M. Radman, M. Meselson, *Proc. Natl. Acad. Sci. USA* **2012**, *109*, 2354.
- [48] R. D. Holbrook, K. E. Murphy, J. B. Morrow, K. D. Cole, *Nat. Nanotechnol.* **2008**, *3*, 352.
- [49] H. U. Dahms, A. Hagiwara, J. S. Lee, *Aquat. Toxicol.* **2011**, *101*, 1.
- [50] C. Ricci, *Hydrobiologia* **2017**, *796*, 277.
- [51] D. B. M. Welch, M. Meselson, *Science* **2000**, *288*, 1211.
- [52] H. Lee, S. M. Dellatore, W. M. Miller, P. B. Messersmith, *Science* **2007**, *318*, 426.

- [53] T. Kiørboe, H. Jiang, R. J. Gonçalves, L. T. Nielsen, N. Wadhwa, *Proc. Natl. Acad. Sci. USA* **2014**, *111*, 11738.
- [54] R. E. Pepper, M. Roper, S. Ryu, P. Matsudaira, H. A. Stone, *J. R. Soc., Interface* **2010**, *7*, 851.
- [55] W. Gilpin, V. N. Prakash, M. Prakash, *Nat. Phys.* **2017**, *13*, 375.
- [56] B. Thallinger, E. N. Prasetyo, G. S. Nyanhongo, G. M. Guebitz, *Biotechnol. J.* **2013**, *8*, 97.
- [57] R. D. Richins, I. Kaneva, A. Mulchandani, W. Chen, *Nat. Biotechnol.* **1997**, *15*, 984.
- [58] F. Soto, R. K. Mishra, R. Chrostowski, A. Martin, J. Wang, *Adv. Mater. Technol.* **2017**, *2*, 1700210.
- [59] S. Cinti, G. Valdés-Ramírez, W. Gao, J. Li, G. Palleschi, J. Wang, *Chem. Commun.* **2015**, *51*, 8668.
- [60] D. A. Uygun, B. Jurado-Sánchez, M. Uygun, J. Wang, *Environ. Sci.: Nano* **2016**, *3*, 559.
- [61] A. Jodra, F. Soto, M. A. Lopez-Ramirez, A. Escarpa, J. Wang, *Chem. Commun.* **2016**, *52*, 11838.
- [62] W. Gilpin, V. N. Prakash, M. Prakash, *J. Exp. Biol.* **2017**, *220*, 3411.